Renewable Energy xxx (xxxx) xxx

Contents lists available at ScienceDirect

Renewable Energy

journal homepage: www.elsevier.com/locate/renene

A field study of ice accretion and its effects on the power production of utility-scale wind turbines

Linyue Gao [a], Tao Tao [b], Yongqian Liu [b], Hui Hu [a, *]

[a] Dept. of Aerospace Engineering, Iowa State University, Ames, IA, 50011-2271, United States
[b] Shool of Renewable Energy, North China Electric Power University, Beijing, 102206, China

ARTICLE INFO

Article history:
Received 8 October 2020
Received in revised form
3 December 2020
Accepted 4 December 2020

Keywords:
Wind turbine icing
Wind farm field campaign
Ice accretion on turbine blades
Icing-induced wind turbine performance degradation
Unmanned-aerial-system (UAS)

ABSTRACT

A field study was conducted to examine ice accretion on 50-m-long turbine blades and icing-induced power production losses to multi-megawatt wind turbines. An unmanned-aerial-system equipped with a digital camera was deployed to take images of the ice structures on turbine blades after undergoing a 30-hour-long icing event to quantify the ice thickness accreted along blade leading edges. While ice accreted over entire blade spans, more ice was found to accrete on outboard blades with the ice thickness reaching up to 0.3 m near blade tips. Based on the icing similarity concept and blade element momentum theory, a theoretical analysis was performed to predict the ice thickness distributions on turbine blades. The theoretical predictions were found to agree with the field measurements well in general. Turbine operation status during the icing event was monitored by using turbine supervisory control and data acquisition (SCADA) systems. Despite the high wind, iced wind turbines were found to rotate much slower and even shut down frequently during the icing event, with the icing-induced power loss being up to 80%. The present study aims to fill in the knowledge gaps between the fundamental icing physics studies conducted under idealized lab conditions and complex wind turbine icing phenomena under realistic, natural icing conditions.

1. Introduction

Wind energy, one of the cleanest renewable power sources, is undergoing a period of rapid growth globally. While the U.S. Department of Energy (DOE) set ambitious yet credible targets of generating 20% of the nation's total electric power demand from wind by 2030 and 35% by 2050, wind power has accounted for about 15% of all European electricity demands in the past year. Wind power installation in China has also been growing by an annual rate of ~10% in recent years and has become the nation's second-largest renewable energy, i.e., only after hydropower. Due to the abundant wind resources and increased air density with the decreasing temperature, the deployment of wind turbines in cold climates has been proliferating in recent years. According to the statistics reported by International Energy Agency (IEA) Wind Proposed Task 19 [1], the cumulative wind installation in cold climates is counting for ~ 30% of the total installed wind power capacity in the world.

Wind turbine icing represents the most significant threat to the integrity of wind turbines in cold climates, which has been found to cause various problems to the safe and efficient operations of wind turbines. Ice accretion on turbine blades will result in decreasing lift and increasing drag [2,3]. Even a light icing event such as frost can produce substantial surface roughness to reduce their aerodynamic efficiency considerably, causing significant turbine power reduction [4,5]. In the case of extreme icing, it may not be possible to start the turbine with subsequent loss of all the potential power production for relatively long periods – resulting in significant energy loss. The icing-induced energy production losses have been found to be more than 20% of the annual energy production (AEP) on many wind farm sites with severe icing [6,7].

It has also been suggested that the operation of a wind turbine with an imbalance caused by randomly accreted ice would impose extra loads on all turbine components. Even though the extreme loads are considered at the design level, the fatigue loads will shorten the lifetime of the turbine components [8]. Wind turbines may stop rotating due to heavy vibrations under uneven ice coverage [9]. The vibrations can also cause large ice chunks to detach. During the ice accretion-and-expulsion process, vibration

* Corresponding author.
E-mail address: huhui@iastate.edu (H. Hu).

https://doi.org/10.1016/j.renene.2020.12.014
0960-1481/

intensity can increase significantly, especially when coupled with strong wind loads, leading to turbine collapses [10,11]. The uncontrolled shedding of large ice chunks is a significant danger to service personnel as well as nearby residents, particularly when the wind farm site borders public roads, housing, power lines, and shipping routes. Ice accretion also affects the reliability of anemometers, thereby leading to inaccurate wind speed measurements and resulting in resource estimation errors [10,12].

Numerous studies have been conducted in recent years to investigate wind turbine icing phenomena. For example, Jasinski et al. [7] conducted an experimental investigation using a conventional wind tunnel to quantify the aerodynamic performance degradation and power output for iced blades using "artificial" iced profiles with various types and amounts of ice accretion. Hochart et al. [8] performed an icing tunnel study to examine the ice accretion process on a turbine blade model experimentally. Gao et al. [3,13–15] conducted a series of experimental studies using an icing research tunnel to characterize the dynamic ice accretion process over the surfaces of turbine blade section models under different icing conditions, and found that the aerodynamic performance degradation induced by the ice accretion would be a strong function of the angle of attack of the turbine blade. Based on the measured aerodynamic forces acting on an iced turbine blade model, Blasco et al. [16] predicted the icing-induced power reduction of a 1.5 MW wind turbine based on a blade element momentum (BEM) theory. Hochart et al. [8] conducted an experimental study to characterize the ice accretion and the resultant lift and drag forces acting on a turbine blade section model. They then scaled the experimental data to a 1.8 MW Vestas wind turbine. Based on the cylinder model and power loss model along with the assumption that a wind turbine would remain continually operational, regardless of the severity of icing events, Lamraoui et al. [17] conducted an analytical study to estimate the power production loss due to the ice accretion on the wind turbine blades theoretically. They found that the power production loss under icing conditions can reach a maximum of 40% at a specific wind speed, regardless of the types of ice accretion. Pedersen & Sorensen [18] presented a Computational Fluid Dynamics (CFD) approach to unify ice accretion modeling and the aerodynamic analysis of the iced object into one CFD-based icing module. Ice accretion on a turbine blade model was simulated under different meteorological boundary conditions to illustrate the capabilities of the CFD-based icing module, and the generated ice shapes showed agreement with the literature. Zanon et al. [19] developed a numerical approach capable of simulating the ice accretion and its effects on wind turbine performance, and applied it to NREL 5 MW reference wind turbine to predict its aerodynamic performance during and after an 8-hour-long icing event. While Parent and Ilinca [20], summarized various state-of-the-art methods for wind turbine anti-/de-icing, Gao et al. [21] suggested a novel hybrid anti-/de-icing strategy to combine an icephobic coating with minimized surface heating near the blade lead edge for wind turbine icing mitigation, and demonstrated the effectiveness of the hybrid strategy experimentally in an icing research tunnel.

It should be noted that, even though the previous studies have uncovered many important findings about wind turbine icing physics most of them were conducted in simplified laboratory settings with the assumptions that wind turbines would encounter uniform winds over a simplified flat surface, remain in same continually operational status, and operate under idealized icing conditions. However, in reality, most wind turbines are sited in wind farms with complex terrains, which are neither flat nor with uniform inflow winds, let alone the complexity and severity of the violent weather changes during icing events (e.g., frozen drizzles, rains, and snowstorms). Quantitative field measurements to characterize ice accretion on wind turbines operating in the realistic, turbulent atmospheric boundary layer (ABL) winds and under natural icing environments are essential to gain further insight into the underlying physics of wind turbine icing phenomena.

Surprisingly, compared to the extensive studies conducted in laboratories, very little can be found in literature about the wind farm field studies to examine ice accretion characteristics on turbine blades and evaluate the icing-induced performance degradation for the wind turbines operating in realistic ABL winds. Rindeskar [22] investigated the possible connections between the ice load and wind turbine production loss by comparing the modeled ice loads for four winters between 2005 and 2009 and the wind farm's power production data. The study was performed with a statistical approach using multiple linear regression and a physical method using an ice accretion model. They found that, while the statistical method is unable to reproduce and predict measured ice loads, the physical model shows more promising results, although with problems in modeling rapid ice accretion and ice shedding events. More recently, Shu et al. [23] conducted a field study to characterize the ice accretion on the blades of a relatively small wind turbine (i.e., turbine rated at 300 KW with 14-m-long turbine blades) under natural icing conditions. They found that the ice accretion on turbine blades would vary significantly along the spanwise direction, with the thickness of the accreted ice layers on the turbine blades increasing rapidly from the blade roots to midspans, and then growing slowly from the midspans to blade tips. While both the pitch angle and rotor speed of the turbine blades were found to decrease remarkably during the icing events, the blade pitch angle shows more sensitive to the ice accretion for the turbine with a traditional control strategy. It should be noted that, since the blade rotation speed of small-sized wind turbines would be much faster than those of the large, multi-megawatt wind turbines commonly seen in modern wind farms, it would lead to significant differences in the inertia effects on the transport process of the impacted supercooled water droplets, thereby, the ice accretion process on surfaces of the rotating turbine blades. Therefore, the icing characteristics revealed from the field measurements of small-sized wind turbines may not be applicable to the large, multi-megawatt wind turbines.

In the present study, we report a Wind Turbine Icing (WTI) field campaign conducted in a 50 MW mountainous wind farm to examine the ice accretion characteristics on 50-m-long turbine blades and to evaluate the icing-induced power production losses of large, multi-megawatt wind turbines during natural icing events. For the WTI field campaign, an unmanned aerial system (UAS) equipped with a high-resolution digital camera was deployed to hover in front of pre-selected wind turbines to acquire snapshot images of the ice structures accreted on the turbine blades right after undergoing icing events. A comprehensive image processing procedure was applied to extract quantitative information from the acquired ice accretion images to characterize the thickness variations of the ice layers accreted along the leading edges (LE) of the turbine blades (i.e., LE ice thickness). Based on the icing similarity parameter concept and blade element momentum (BEM) theory along with the known geometric information of the turbine blades, a theoretical analysis was also performed to predict the LE ice thickness distributions over the turbine blades, and the theoretic predictions were validated against the field measurement data quantitatively. In addition to using the UAS-based imaging system to examine the ice accretion characteristics on the turbine blades, the operational status of the wind turbines was also monitored during the icing events by using supervisory control and data acquisition (SCADA) systems in terms of the incoming wind speed, rotational speed and pitch angle of the turbine blades, and the power production data. By comparing the SCADA measurement

data acquired during the icing event against those under normal operating conditions without ice accretion, the effects of the ice accretion over turbine blades on the turbine operation status as well as the icing-induced power production loss of large, multi-megawatt wind turbines were evaluated quantitatively.

To the best knowledge of the authors, the work presented here represents the first field campaign conducted in a large wind farm to examine the ice accretion characteristics over the entire blade spans of large, multi-megawatt turbines and to evaluate the effects of the ice accretion on the operation status and power production losses of the utility-scale wind turbines systematically. The present study aims to fill in the knowledge gaps between the fundamental icing physics studies performed in laboratories with simplified, small 2-D turbine blade models under idealized testing conditions and the complicated ice accretion phenomena on large, utility-scale wind turbines siting in wind farms with complex terrains under violent natural icing conditions. It will lead to a better understanding of the characteristics of the ice accretion on wind turbines operating under realistic icing conditions, which is very helpful and essential to improving current icing accretion models for more accurate predictions of wind turbine icing phenomena and development of effective anti-/de-icing strategies for the safer and more efficient operation of wind turbines in cold climates.

2. Wind farm site for the field campaign and measurement instrumentations

2.1. Wind farm site and large, utility-scale wind turbines

The WTI field campaign was conducted in a wind farm located in Anhui Province of China, composed of 31 sets of 1.5 MW wind turbines and two sets of 2.0 MW wind turbines. As shown in Fig. 1, wind turbines are sited along the ridges of mountains due to the abundant wind resources and favorable accessibility at the sites. The altitudes of the wind turbine sites range from ~1100 m to ~1800 m above the sea level. Based on the historical data recorded by local meteorological stations from 1957 to 2009, there are approximately 70 icing days per year during the winters at the wind turbine sites. Since the wind farm was built in 2016, the wind turbines were reported to encounter various icing events in winters mainly from December to February, including in-cloud icing (i.e., freezing fog, as shown in Fig. 1(b)), and precipitation icing (i.e., freezing rain, freezing drizzle, or wet snow). At the time when the pictures in Fig. 1(b) were taken, it was foggy with a high moisture level in the air. Since the ambient temperature on the top of the mountain was well below the water freezing point (i.e., $T_{ambient} \approx -3.5\ ^{\circ}C$) at the moment, the water droplets suspended in the air would be in a supercooled state (i.e., freezing fog). Upon impacting the surfaces of the rotating turbine blades, the impacted supercooled water droplets would turn into ice immediately to start ice accretion on the surfaces of the turbine blades. In addition, the precipitations, such as freezing drizzle, freezing rain, sleet, and wet snow, were also found to lead to ice accretion on the turbine blades.

The 1.5 MW wind turbines on the wind farm were selected for the WTI field campaign. The wind turbines are variable-speed & variable-pitch regulated in upwind turbine arrangement with the rotor diameter being 100 m and a hub height of 78 m. All three blades of each wind turbine were collectively controlled, i.e., always having the same pitch angles during the operation. As shown schematically in Fig. 2, the designed power curve for the 1.5 W M wind turbines under normal operation conditions (i.e., without ice accretion) can usually be divided into four operational regions, depending on the incoming wind speed. In Region I, since the incoming wind speed is lower than the designed cut-in speed of 2.8 m/s, the wind turbine cannot start due to the lack of sufficient torque generated by the turbine blades under the low wind conditions. When the incoming wind speed falls between the cut-in and rated wind speeds, i.e., 2.8 m/w ~8.9 m/s in Region II, the wind turbine would be in rotational-speed-regulated mode (i.e., as the incoming wind speed increases, the blade rotational speed would also increase correspondingly). When the wind turbine operates in Region II, the blade pitch angle would usually be small (i.e., 0° ~ 3°) to achieve the optimum power output. When the

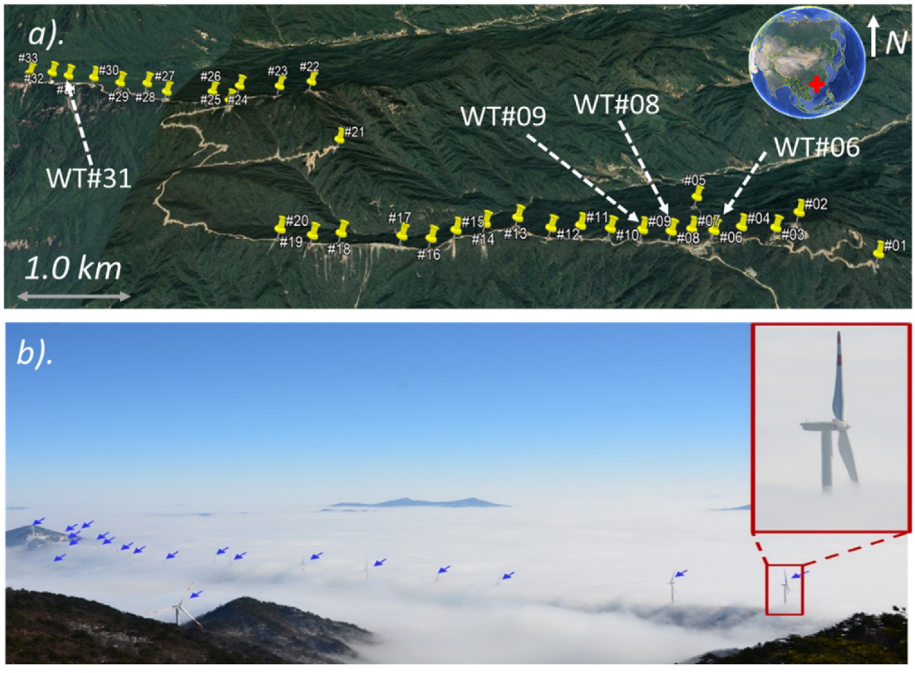

Fig. 1. Photos of the wind turbines sited in a wind farm located in Anhui province of China. (a) The layout of the wind farm; (b) the photo of the wind turbines in freezing fog.

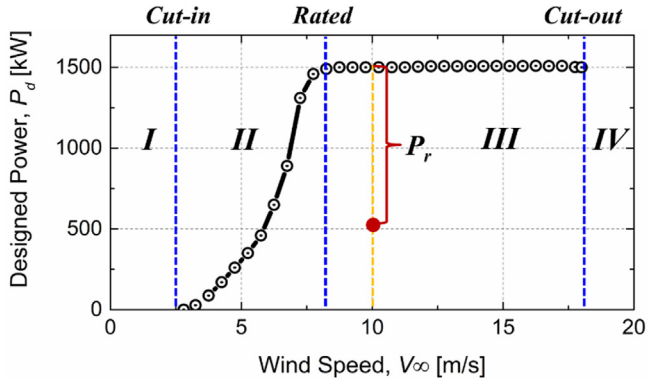

Fig. 2. Designed power curve of the wind turbines investigated in the WTI field campaign.

incoming wind speed falls in between the rated and cut-out wind speeds, i.e., 8.9 m/s ~18.0 m/s in Region III, the wind turbine would be in pitch-regulated mode with a fixed blade rotation speed. As the wind speed increases, the blade pitch angle would also increase correspondingly to limit the power output, ensuring the safe and efficient operation of the wind turbine under high wind conditions. When the incoming wind speed is beyond the designed cut-out speed, i.e., >18.0 m/s in Region IV, the wind turbine would be shut down for the sake of turbine safety. Table 1 summarizes the primary technical parameters of the 1.5 MW wind turbines investigated in the present study.

Fig. 3 shows the schematic of the 50-m-long blade of the large, utility-scale wind turbines. It can be seen clearly that, while the turbine blade are designed to have a circular-shaped cross-section (i.e., 2.00 m in diameter) at the root to provide strong support to overcome the significant structural loads (i.e., torsion forces and bending moment), the cross-section profiles in the outboard region of the blade are aerodynamically optimized (i.e., with different airfoil profiles changing from DU400 to DU350, then DU300 to DU250 in the mid-span; and final from NACA63_421 and NACA63_618 in the tip region) to ensure good performance for wind energy harvesting [24]. As shown quantitatively in Fig. 3(b), the blade has a chord length of 2.0 m at the blade root (i.e., in the circular shape) and becoming only about 0.2 m near the blade tip. The maximum chord length of $C_{max} = 3.62$ m is designed to be in the cross-section of $r/R = 0.20$. Fig. 3(c) reveals that the maximum thickness of the turbine blade would decrease gradually from 2.0 m at the blade root to being about 0.02 m at the blade tip. It should also be noted that there are several "arrow" marks pre-printed on the blade, as shown clearly in Fig. 3(a), which were used as the reference points to align the snapshot images of the blade sections acquired by using a UAS-based imaging system for the WTI field campaign.

2.2. UAS based imaging system to acquire ice accretion images on turbine blades

For the WTI field campaign, a commercially available UAS (i.e., DJI Mavic Air 4K) equipped with a high-resolution digital camera (spatial resolution 4056 pixels × 3040 pixels) and a 3-axis gimbal platform was used to acquire the snapshot images of the ice structures accreted on pre-selected turbine blades. As shown in Fig. 4, the UAS was programed to hover in front of the pre-selected wind turbines to acquire snapshot images of the ice structures accreted on the turbine blades. By adjusting the UAS hovering height and/or manipulating the 3-axis gimbal platform, high-resolution images of the turbine blades can be acquired at any selected sections. As demonstrated in Fig. 4(c), by properly aligning the acquired blade section images, the 50-m-long turbine blade was imaged with a reasonably good spatial resolution (i.e., ~3.5 mm/pixel).

Fig. 5 gives an example of the snapshot images acquired by using the UAS-based imaging system to reveal the ice accretion on the surface of a pre-selected turbine blade of a wind turbine (i.e., WT#09 indicated in Fig. 1) right after undergoing an icing event with about 30 hours in duration (i.e., the icing event shown in Fig. 10). Using the "arrow" marks pre-printed on the blade at known radial locations as the references, the acquired images of different blade sections were appropriately aligned to form a combined vision to reveal the ice accretion over the entire 50-m-long span of the turbine blade. Based on the acquired ice accretion images as those given in Fig. 5, the quantitative information about the ice layer accreted along the leading edge of the blade can be extracted via an image processing procedure to be introduced in the next section.

2.3. Monitoring turbine operational status with turbine SCADA data

In addition to acquiring snapshot images of the ice accretion on the turbine blades by using the UAS-based imaging system to examine the ice accretion characteristics on the turbine blades, the operational status of the wind turbines under natural icing conditions was also monitored by using turbine supervisory control and data acquisition (SCADA) systems. While SCADA systems have been widely used to monitor the operation status of the wind turbine for various applications [25–27], the quantitative measurement data provided by the SCADA systems for the present WTI field campaign include the time histories of the incoming wind speed measured by using heated anemometer sensors at the turbine hub height, pitch angle, rotational speed of the turbine blades, and the corresponding power output data of the wind turbines. By correlating the characteristics of the ice accretion over the turbine blades revealed from the ice accretion images acquired by using the UAS-based imaging system and the quantitative measurement data of the SCADA system about the operational statue and power production data of the wind turbines, the effects of the ice accretion over the turbine

Table 1
Primary technical parameters of the large, utility-scale wind turbines.

Turbine rated power [MW]	1.50
Wind turbine type	upwind, variable-speed, variable-pitch
Blade number	3
Rotor diameter [m]	100
Hub height [m]	78
Cut-in, rated, and cut-out wind speed [m/s]	2.8, 8.9, and 18.0
Rated rotational speed [rpm]	15
Rotational direction	clockwise

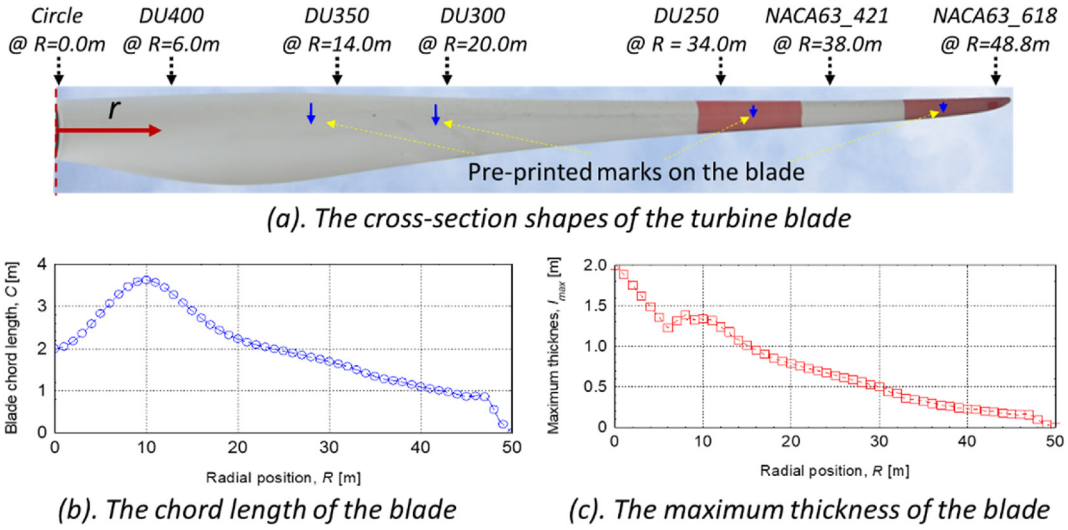

Fig. 3. The primary geometric parameters of the turbine blade.

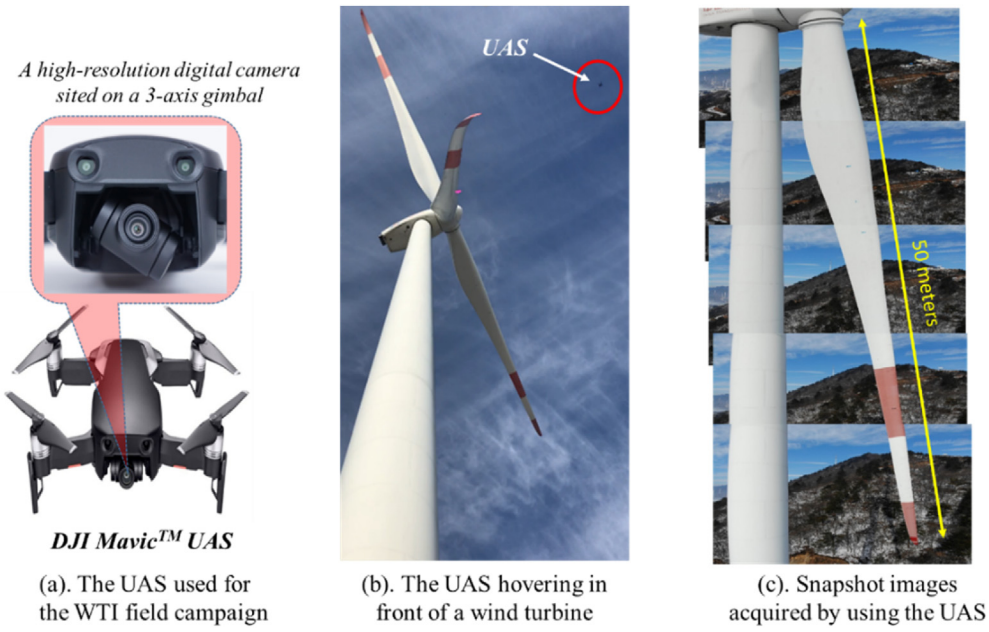

Fig. 4. The UAS-based imaging system used in the present study for the WTI field campaign.

blades on the operation status and the icing-induced power product losses of the wind turbines were revealed clearly and quantitatively.

3. Measurement results and discussions

3.1. Quantification of ice accretion characteristics along the entire span of turbine blades

While there are 34 wind turbines sited in the wind farm, most of the measurements for the WTI field campaign were carried out for four wind turbines (i.e., WT#06, WT#08, WT#9, and WT#31 as indicated in Fig. 1) due to their good accessibility. Based on the outputs of the icing sensors mounted on the top of the turbine nacelles, the durations of the icing periods experienced by the wind turbines are 25.4 hours, 25.6 hours, 30.6 hours, and 6.7 hours within the four days of the WFI field campaign for WT#06, WT#08, WT#09, and WT#31, respectively. Due to the continuous or intermittent ice accretion process, the total amount of the ice accreted on turbine blades was found to increase continuously with the duration of the encountered icing events. The UAS was launched right after the icing events to hover in front of the wind turbines to take snapshot images of the iced turbine blades at different radial sections. While very similar ice accretion features were revealed from the acquired images of the iced turbine blades, only the measurement results for WT#08 and WT#09 were given here for conciseness. Table 2 lists some of the measured key parameters when the UAS was launched to acquire ice accretion images on the turbine blades of WT#08 and WT#09.

Fig. 5 gives the typical snapshot images of the ice accretion on a pre-selected turbine blade of WT#09. It can be seen clearly that, while ice accretion was found to take place over the entire span of

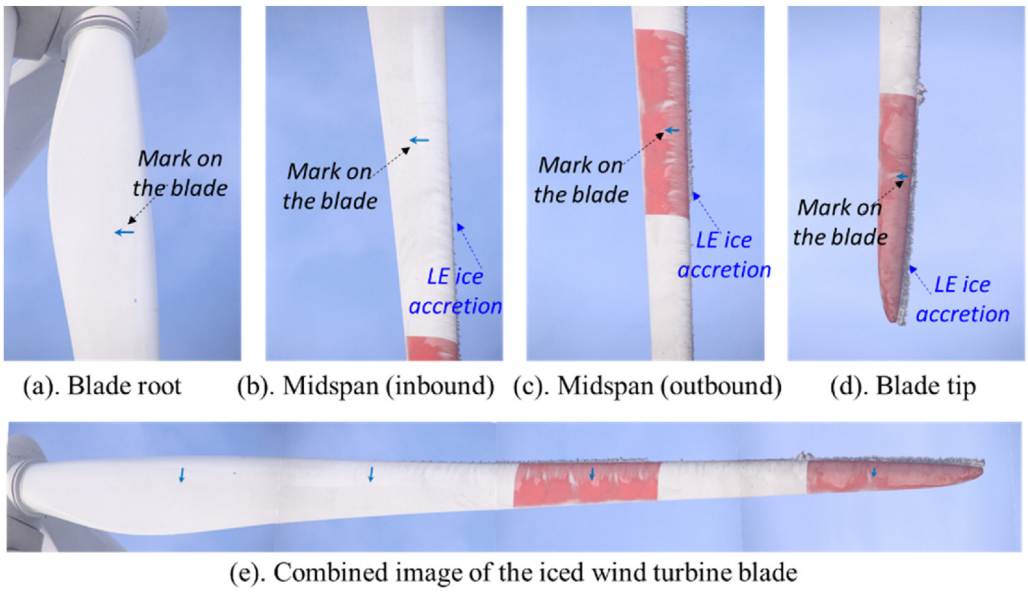

Fig. 5. Typical images of an iced blade acquired by using the UAS-based imaging system.

Table 2
Key parameters when the UAS was launched to acquire images of iced turbine blades.

WT No.	V_∞ [m/s]	Ω [rpm]	T_∞ [°C]	RH [%]	Icing duration (hours)
WT#08	5.48	8.60	−3.40	89.20	25.6
WT#09	5.04	8.76	−3.40	89.20	30.6

the turbine blade, much more ice structures were found to accrete in the outbound region of the turbine blade, especially near the blade tip, in comparison to those in the inbound region (i.e., near the blade root). It can also be seen that ice structures are accreted mainly along the leading edge (LE) of the turbine blade.

As described in Shu et al. [23] and Gao et al. [13], the thickness of the ice layer accreted along the leading edge of a turbine blade can be used as a quantitative indicator to represent the seriousness of the ice accretion on the turbine blade. Lamraoui et al. [17] also suggested that the wind turbine power reduction caused by the ice accretion would be closely related to the thickness of the ice layers accreted along the leading edges of the wind turbine blades, regardless of the type of ice (i.e., either rime or glaze icing). In the present study, an image processing procedure was developed to extract quantitative information from the acquired ice accretion images to characterize the thickness variations of the ice layers accreted along the leading edges (LE) of the wind turbine blades.

Fig. 6 shows one example to demonstrate how the acquired ice accretion images were processed to determine the LE ice thickness distributions on the turbine blades. A set of image processing algorithms [28,29], including Gaussian filtering for noise reduction, background removing, binary treatment for edge enhancing, and a Canny algorithm for edge detection, were used to process the image of the iced blade given in Fig. 6(a). As shown clearly in Fig. 6(b), both the leading and trailing edges of the turbine blade and the outer profile of the ice layer accreted along the leading edge of the wind turbine blade were detected nicely as the outputs of the image processing procedure. It should be noted that, while the ice structures accreted on the wind turbine blades are highly three-dimensional with complex topological features, the outlines of the ice layer extracted from the acquired ice accretion image given in Fig. 6 would represent the outmost profile of the ice layer accreted along the leading edge of the turbine blade.

Similar to the work described in Shu et al. [23], with the known information about the local chord length distribution of the turbine blade and the radial locations of the pre-printed marks as given in Fig. 3, the scaling factors between the image domain of the acquired ice accretion images and the physical domain, $F_{scaling}$, can be determined for each acquired ice accretion images, which is expressed as:

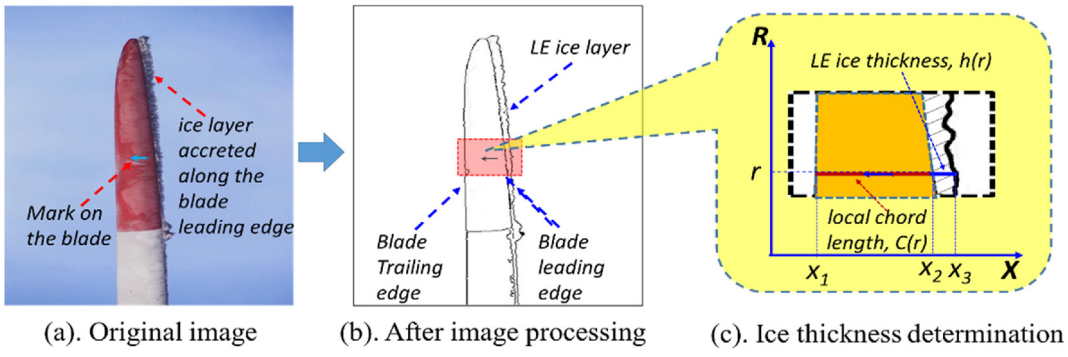

Fig. 6. Determination of ice thickness along the blade leading edge from the acquired images.

$$F_{scaling} = C(r) \Big/ (x_2 - x_1) \quad (1)$$

where $C(r)$ is the local chord length of the turbine blade at the radial location of r; x_1 and x_2 are the pixel coordinates of the trailing and leading edges of the turbine blade in the acquired iced blade image. After the scaling factors, $F_{scaling}$, were determined, the pixel coordinates in the acquired ice accretion image can be converted into physical space on a pixel-by-pixel basis. Then, the local thickness of the ice layer accreted along the leading edge of the turbine blade (i.e., LE ice thickness) can be determined as:

$$h(r) = F_{scaling}(x_3 - x_2) \quad (2)$$

where x_3 is the pixel coordinate of the outmost edge of the accreted ice layer in the acquired image.

By applying the image processing procedure described above to all the acquired ice accretion images, the LE ice thickness variations along the entire span of the turbine blades can be determined quantitatively. Fig. 7 gives the measured LE ice thickness distributions as a function of the radial locations away from the blade roots for the two pre-selected turbine blades on WT#08 and WT#09. It was revealed quantitatively that the measured thickness of the ice layers accreted along the leading edges of the turbine blades increased monotonically along the radial direction of the turbine blades (i.e., from the blade root to tip). More specifically, while the ice thickness values in the region near the turbine roots were found to be small (i.e., almost negligible), the measured LE ice thickness value near the blade tip of WT#08 was found to be about 200 mm after undergoing the 25.6-hour-long icing event. Corresponding to the longer duration of the icing event experienced by WT#09 (i.e., 30.6-hour-long icing event), the thickness of the ice layer accreted near the blade tip was found to increase to about 300 mm. The monotonic increase feature revealed from the measured LE ice thickness along the turbine blades can be explained by the fact of that, after experiencing the same duration of the icing event, since the sweeping area for a blade element on the turbine blade would increase with the increasing radius away from the rotation center (i.e., blade root), more airborne supercooled water droplets would be collected by the blade element located at the outer bound of the rotating blade, in comparison to that at the inner bound of the blade. The greater accumulated water mass would result in more ice accretion at the outbound of the turbine blade (i.e., near the blade tip) than that at the inbound (i.e., near the blade root). It should also be noted that, as indicated by the dashed lines given in Fig. 7, the variations of the measured LE ice thickness data along the spanwise direction of the turbine blades were found to be fitted reasonably well by using parabolic functions.

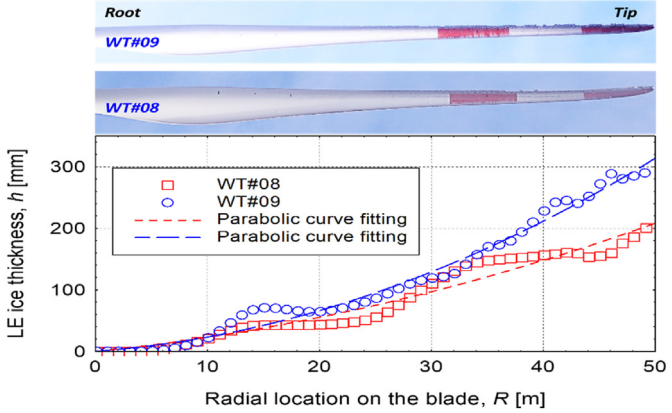

Fig. 7. The measured LE ice thickness as a function of the radial location on the turbine blades.

As aforementioned, while extensive studies have been conducted to investigate wind turbine icing in recent years, most of the previous studies were performed in laboratories with simplified 2-D turbine blade section models (i.e., the test models with identical airfoil profile in the cross-sections and same chord length and thickness in the spanwise direction) and rather uniform incoming airflows. Therefore, it will be very difficult, if not impossible, to examine the variation characteristics of the ice accretion along the spanwise direction of rotating turbine blades by conducting lab experiments in either conventional wind tunnels or icing research tunnels. However, as shown clearly in Fig. 3, cross-section shapes, airfoil thickness, and chord length of a utility-scaled turbine blade would change significantly from the blade root to tip. Furthermore, for a rotating turbine blade, the relative velocity of the incoming airflow for a blade element on the blade would nearly increase linearly with the increasing radial distance away from the rotation center (i.e., blade root). As a result, the ice structures accreted on the turbine blade at different radial positions are expected to vary significantly from the blade root to tip. By conducting a field study of the ice accretion on the blades of a small wind turbine (i.e., turbine rated at 300 KW with 14-m-long turbine blades), Shu et al. [23] found that the LE ice thickness on the blades of the small-sized wind turbine would increase rapidly from the root to the midspan, and then growing slowly from the midspan the blade tips, which is different from the variation characteristics of the LE ice thickness revealed from the field measurement results of the present study given in Fig. 7. The discrepancy can be explained by the fact that the much faster rotation speed of the smaller wind turbine studied by Shu et al. [23] would lead to significant differences in the inertia effects on the transport process of the impacted supercooled water droplets, thereby, changing the ice accretion characteristics on the rotating turbine blades, as described in Gao et al. [13]. Battisti [30] also suggested that the blades of small-sized wind turbines could be evenly wetted on the whole span, while the wetted regions on turbine blades could increase dramatically as the blade radius position increases for larger wind turbines. It should also be noted that the measurement data given in Fig. 7 are believed to be the first quantitative field measurement results to reveal the characteristics of the ice accretion along the entire blade span of large, utility-scale wind turbines commonly seen in modern wind farms.

3.2. Theoretical analysis to predict ice accretion on turbine blades

In addition to conducting field measurements, a theoretical analysis was also performed in the present study to predict the ice accretion characteristics along the spanwise direction of turbine blades. As described in Anderson [31] and Waldman and Hu [29], an icing similarity parameter, named ice accumulation parameter, is usually used to characterize the ice accretion over the airfoil surface of an arbitrarily-selected blade element on a rotating turbine blade. Following the work of Anderson [31], the ice accumulation parameter, A_c, is defined as:

$$A_c = \frac{LWC \cdot V_{rel} \cdot t}{\rho_i \cdot l} \quad (3)$$

where LWC refers to the liquid water content in the incoming airflow; V_{rel} is the incoming airflow velocity; t is the ice accretion time; ρ_i is the ice density; and l is the characteristic length of the airfoil. As reported in Gao et al. [13], since the thickness of the ice layer accreted along the leading edge (i.e., LE ice thickness) of a turbine blade model would be linearly related to the value of the ice

accumulation parameter, A_c, under various icing conditions (i.e., rime, glaze and mixed), the variations of the ice accumulation parameter over a turbine blade span can be used to predict the LE ice thickness distribution along the spanwise direction of the turbine blade theoretically.

For the scenario of the present study, *LWC*, ρ_i, and t mainly depends on local meteorological conditions during the icing event. The variations of these parameters at different radial locations on the same turbine blades are very small and negligible. The value of l refers to the maximum thickness of the selected blade element on the turbine blade. As shown schematically in Fig. 8, according to the blade element momentum (BEM) theory [32], the relative airflow velocity, V_{rel}, seen by a blade element on a rotating turbine blade would consist of an inflow velocity component, $V_\infty(1-a)$, and a rotational velocity component $\Omega r(1+a')$, which can be expressed as:

$$V_{rel} = (V_\infty(1-a))[(V_\infty(1-a))^2 + (\Omega r(1+a'))]^{1/2} \quad (4)$$

where V_∞ refers to the freestream airflow velocity approaching the blade element, which was set to be the hub-height wind speed measured by using an anemometer on the top of the turbine nacelle in the present study without considering the wind shear effects at different elevations along the blade span. Ω refers to the rotational angular velocity of the turbine blade, which was recorded by using a SCADA system during the field campaign. While r is the radial position of the blade element away from the rotation center (i.e., turbine root), a is the axial induction factor that represents the reduction of the incoming airflow velocity due to the momentum exchange between the wind and the turbine. a' is the tangential induction factor that captures the increase in Ωr due to the wake rotation. In the present study, with the known geometric information of the turbine blade given in Fig. 3, the values of the axial and tangential induction factors (i.e., a and a') were determined interactively by using a BEM algorithm similar to that used by Johnson et al. [33]. While the values of the axial induction factor, a, were found to increase gradually from blade root to the tip with $a = 0.33$ in the cross-section located at about 70% of the blade span, the values of the tangential induction factor, a', were found to decrease gradually from the blade root to the tip, becoming almost zero at the blade tip. It should also be noted that the icing-induced effects on the variations of a and a' were not considered in the theoretical analysis of the present study.

With the known geometric information about the turbine blade (e.g., the chord length and blade thickness distributions given in Fig. 3) and the relative airflow velocity seen by an arbitrarily selected blade element on the turbine blade given by Eq. (4), the variations of the ice accumulation parameter, A_c, over the entire blade span can be determined by using Eq. (3). Since the value of the ice accumulation parameter, A_c, would be linearly related to the LE ice thickness on the turbine blade as reported by Gao et al. [13], the variations of the LE ice thickness along the spanwise direction of the turbine blade can be predicted theoretically based the distribution of the ice accumulation values at different radial locations on the turbine blade.

As aforementioned, since the variations of the meteorological parameters of *LWC*, ρ_i, and t at different radial locations of the same turbine blade were assumed to be negligible, a normalization operation (i.e., normalized by the ice accumulation parameter at the blade tip) was implemented in the present study to determine the normalized ice accumulation parameter, which is expressed as:

$$\overline{A_c(r)} = \frac{A_c(r)}{A_{c,tip}} = \frac{V(r)/l(r)}{V_{tip}/l_{tip}} \quad (5)$$

With the introduction of $\overline{A_c(r)}$, the effects of the meteorological parameters of *LWC*, ρi, and t on the theoretical analysis of the ice accretion can be eliminated.

In order to provide a quantitative comparison to the theoretical prediction of the LE ice thickness distribution in the term of normalized ice accumulation parameter of $\overline{A_c(r)}$, the measured LE ice thickness data obtained through the WTI field campaign were first divided by the local chord length of the blade element (i.e., h/c) to account for the effects of the local chord length on the ice accretion process, and then normalized by the value at the blade tip in the form of Eq. (6).

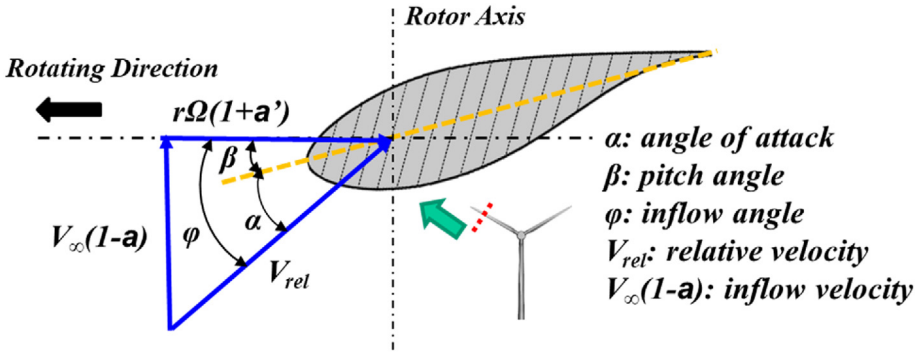

Fig. 8. Schematic of blade element theory to analyze wind turbine aerodynamics.

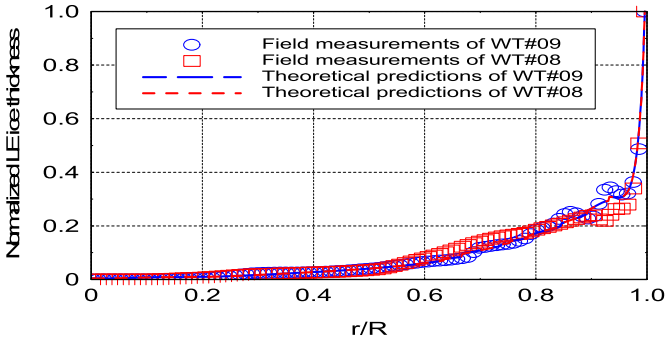

Fig. 9. Comparisons between the field measurements and theoretical predictions in determining the normalized LE ice thickness distributions along the blade span of WT#08 and WT#09.

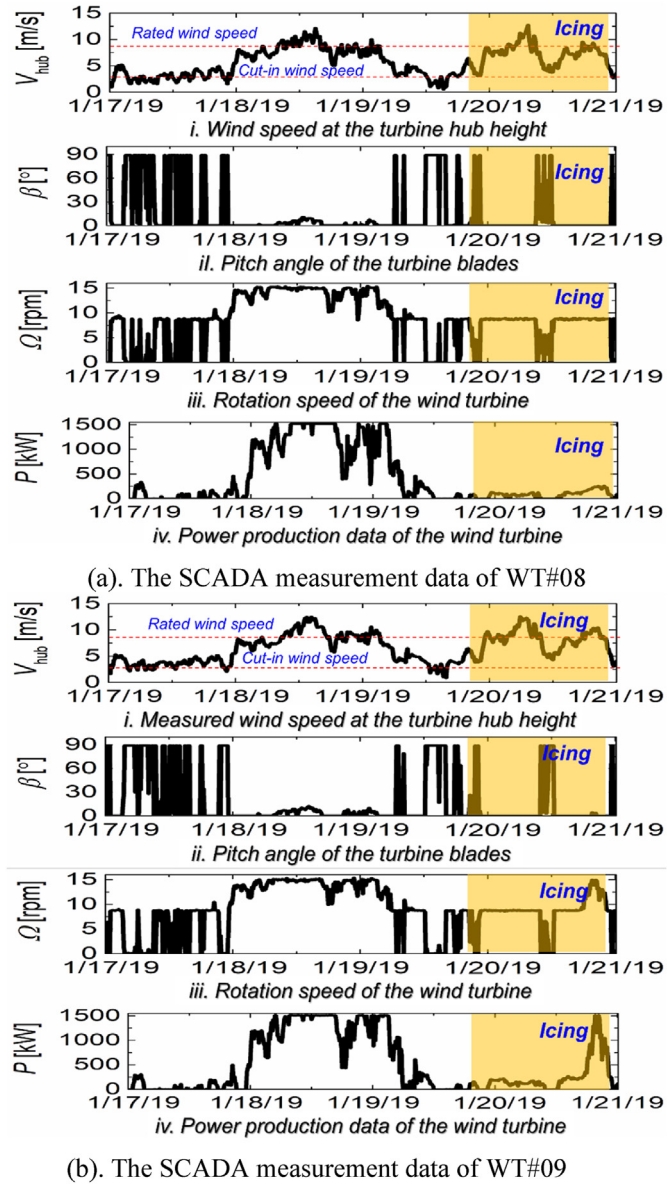

Fig. 10. The operational status of WT#08 and WT#09 during the 4-day interrogation period.

$$\overline{h(r)} = \frac{h(r)/C(r)}{h_{tip}/C_{tip}} \tag{6}$$

Fig. 9 shows the quantitative comparison between the field measurement results (i.e., in terms of $\overline{h(r)}$) and the theoretical predictions (i.e., in the term of $\overline{A_c(r)}$) of the normalized LE ice thickness as a function of the radial location away from the blade root for the blades of WT#08 and WT#09. It can be seen clearly that, while the theoretic prediction results were found to agree reasonably well with the field measurement data in general, the theoretical predictions yield much smoother curves in comparison to the field measurement results. Some apparent discrepancies could also be identified between the field measurement data and the theoretical prediction results, especially in the outbound regions (i.e., $r/R > 0.6$). The discrepancies are believed to be caused by several assumptions/simplifications used in the theoretical analysis, including no turbulence effects and uniform incoming airflow (i.e., no wind shear across the 50-m-long blade span), no variations of a and a' due to ice accretion, and negligible variations of the meteorological parameters (i.e., LWC, ρ_i, and t), etc. Additionally, the more readily shedding of ice chunks from the outbound region of the turbine blades during the icing events was also not considered in the theoretical analysis in determining the normalized ice accumulation parameter of $\overline{A_c(r)}$.

3.3. Characterization of the performance degradation of wind turbines due to ice accretion

In addition to using the UAS-based imaging system to acquire images of the iced blades to determine ice accretion characteristics on the turbine blades, the effects of the ice accretion on the operation status and power production performances of the wind turbines were also examined based on the quantitative measurement data of the turbine supervisory control and data acquisition (SCADA) systems during the 4-day WFI field campaign (i.e., from midnight of January 17, 2019 to midnight of January 21, 2019 local time). While very similar characteristics of the ice accretion effects were revealed from the recorded SCADA data for all the studied wind turbines, only the measurement data for WT#08 and WT#09 were given here for conciseness.

Fig. 10 gives the time histories of the recorded primary operation parameters of WT#08 and WT#09 during the 4-day interrogation period in terms of the incoming wind speed measured at the turbine hub height (V_∞), blade rotational speed (Ω), pitch angle (β) of the turbine blades, and power production output (P) of the wind turbines. The time interval for the data acquisition of the SCADA system is 10 min. It can be seen clearly that, while the incoming wind speed (V_∞) fluctuated greatly during the interrogation period due to the turbulence nature of the incoming atmospheric boundary layer (ABL) airflow over the wind farm, the corresponding power production outputs of the wind turbines were also found to vary significantly, as expected. When the measured incoming wind speed is lower than the cut-in speed (i.e., $V_{hub} < 2.8$ m/s and within Region I as shown schematically in Fig. 2), the wind turbines were found to be in a standstill status with zero turbine rotational speed ($\Omega = 0$ rpm), and the turbine blades were in the feathering status with the blade pitch angle of $\beta = 90°$ for the low wind periods on 01/17/2019 local time. It was also revealed clearly that, as the incoming wind speed is within the range from cut-in wind speed (i.e., $V_{hub} > 2.8$ m/s) to the rated wind speed (i.e., $V_{hub} = 8.9$ m/s) for the most of time on 01/18/2019 and 01/19/2019 local time, i.e., within Region II shown in Fig. 2, the higher incoming wind speed would result in stronger aerodynamic forces acting on

the turbine blades. As a result, greater torques would be generated to drive the turbine blades to rotate with faster rotational speeds, thereby resulting in higher power outputs from the wind turbines, as shown quantitatively in Fig. 10. It can also be seen that when the incoming wind speed exceeded the rated wind speed (i.e., V_{hub} > 8.9 m/s in the early morning of 01/19/2019 local time), while the power production values of the wind turbines were found to remain at their maximum output value of 1.5 MW, the pitch angles of the turbine blades were found to increase gradually in order to reduce the significant wind loads acting on turbine blades during the high wind periods, i.e., corresponding to Region III shown in Fig. 2.

The wind turbines were also found to encounter an icing event during the 4-day interrogation period, which is highlighted in yellow shade given in Fig. 10. During the icing event, while the ambient temperature at the wind turbine sites was found to be below the water frozen temperature (i.e., fluctuating from $T_{ambient} \approx -2.0$ °C to $T_{ambient} \approx -7.5$ °C), incoming airflow was quite wet with relatively high humidity (RH) or/and liquid water content (*LWC*) values (i.e., RH values varying from about 75% to 100%). As shown clearly in the highlighted icing region given in Fig. 10, since the incoming wind speed was always relatively high during the icing event (i.e., well above the turbine cut-in speed of 2.8 m/s), the wind turbines are supposed to have relatively high power production if no ice accretion would be taken place on the turbine blades. However, as revealed quantitatively from the SCADA measurement data given in Fig. 10, while the wind turbines were still found to rotate for most of the time during the icing event, the corresponding power production outputs of the wind turbines were found to be very low in general, despite the relatively high incoming wind speed. This can be explained by the fact that, since ice accretion on the turbine blades would degrade the aerodynamic performance of the blades significantly (i.e., decreasing lift and increasing drag) as reported by Jasinski et al. [7] and Gao et al. [3], even though the incoming wind speed is high during the icing event, only limited torques could be generated by the iced blades. As a result, while the turbines were found to rotate much slowly (i.e., with much lower rotational speeds), the power outputs of the wind turbines were found to become much lower during the icing event, in comparison to those under normal operating conditions (i.e., without ice accretion), as revealed quantitatively from the SCADA measurement data given in Fig. 10.

It can also be seen that, even though the incoming wind speed was well above the cut-in wind speed of 2.8 m/s during the entire icing event, the wind turbines were found to stop rotating from time to time. This is because the generated torques were too low to drive the wind turbines to rotate. Therefore, the turbine rotational speed was found to decrease down to 0 rpm, and the corresponding pitch angle of the turbine blades increased up to 90° when the turbines were in shutdown mode, as shown quantitatively in Fig. 10. It indicates that, despite the abundant wind energy resource available during the icing event (i.e., as indicated by the measured high speed of the incoming wind approaching the wind turbines), ice accretion on the turbine blades would cause the wind turbines to shut down completely with no wind energy being harvested at all. This is highly undesirable since the electricity is usually in high demand and at its highest price during the cold icing seasons [34]. It should be noted that the snapshot images of the iced turbine blades given in Fig. 5 were taken right after the icing event on 01/21/2019 of the local time.

In order to reveal the effects of the ice accretion over turbine blades on the power production capacities of the wind turbines more clearly, the measured power production data of four selected wind turbines, i.e., WT#06, WT#08 WT#09, and WT#31, were replotted as a function of the measured wind speed at the turbine hub height during the period of the icing events, as shown in Fig. 11. The designed power production curves of the 1.5 MW wind turbine were also given in the plots as the comparison baseline. It can be seen clearly that the measured power production outputs of the wind turbines during the icing events were found to be significantly lower than the designed values. It confirms that ice accretion over turbine blades would substantially reduce the power production of the wind turbines.

A non-dimensional parameter, named averaged power production loss factor, is introduced in the present study to quantify the significance of the turbine power loss due to the ice accretion on turbine blades, which is defined as in Eq. (7).

$$\eta_p = \frac{1}{T}\int_0^T \left(1 - \frac{P_{measured}}{P_d}\right) dt \times 100\% \tag{7}$$

where T is the duration of the icing event; $P_{measured}$ is the measured turbine power production value during the icing event, $P_d$is the nominal power production value of the wind turbine at the same incoming wind speed according to the designed power production curve of the wind turbine.

Based on the measured turbine power production data given in Fig. 11, the averaged power production loss of the wind turbines can be determined. It was found that the icing-induced power production losses would increase with the duration of the icing events significantly. As shown in Fig. 1, since WT#31 is located quite far from the other three wind turbines and had a much shorter icing duration (i.e., the icing event only last 6.5 hours at the site of WT#31), ice accretion on the blades of WT#31 was found to be much less than those of the other three wind turbines. As a result, the averaged icing-induced power production loss for WT#31 was found to be only about 20% (i.e., a wind power loss of 1,053 kWh out of 5,263 kWh nominal wind power), which is the lowest among the four studied wind turbines. While the averaged icing-induced power production loss for WT#06 was found to be about 77% (i.e., a wind power loss of 8,822 kWh out of 11,458 kWh nominal wind power) over the 25.4-hour-long icing event, the corresponding value for WT#08 was found to be about 78% (i.e., a wind power loss of 10,704 kWh out of 13,723 kWh nominal wind power) with almost the same duration of the experienced icing event (i.e., 25.6-hour-long icing event). Corresponding to the longest icing duration experienced by WT#09 (i.e., 30.6-hour-long icing period), WT#09 was found to have the most severe ice accretion on the turbine blades (i.e., the LE ice thickness at blade tip being about 300 mm for WT#09 as shown in Fig. 4). The averaged icing-induced power production loss for WT#09 was found to be the highest among the four studied turbines, reaching more than 80% (i.e., a wind power loss of 9,772 kWh out of 12,215 kWh nominal wind power). It indicates that WT#09 would only be able to generate less than 20% of its designed power during the 30.6-hour-long icing event.

4. Conclusions

A Wind Turbine Icing (WTI) field campaign was conducted in a 50 MW mountainous wind farm to investigate the ice accretion characteristics on the 50-m-long turbine blades and to evaluate the effects of the ice accretion on the operation status and power production capacities of utility-scale wind turbines. An unmanned-aerial-system (UAS) equipped with a high-resolution digital camera was deployed to hover in front of the pre-selected wind turbines to acquire snapshot images of the ice structures accreted on the turbine blades right after undergoing icing events. A comprehensive image processing procedure was used to extract quantitative

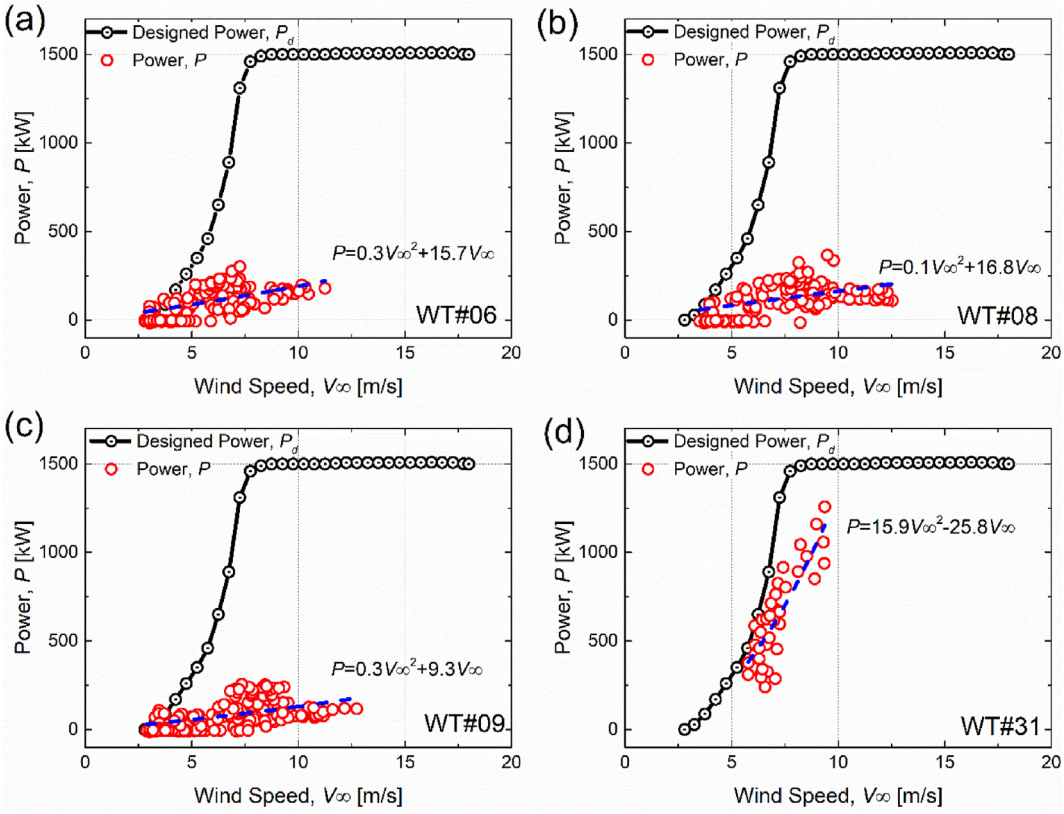

Fig. 11. The measured turbine power production data as a function of the measured hub height wind speed during the icing event for (a) WT#06; (b) WT#08; (c) WT#09; and (d) WT#31.

information from the acquired ice accretion images to characterize the thickness variations of the ice layers accreted along the leading edges (LE) of the turbine blades (i.e., LE ice thickness distributions). While ice accretion was found to take place over the entire span of the 50-m-long turbine blades, much more ice was found to accrete in the outbound regions of the blades (i.e., near blade tips) than those in the inbound regions (i.e., near blade roots), which correlated well with the greater sweep area of the blade elements in the outbound regions of the turbine blades. The ice layers accreted near blade tips were found to have the maximum thickness, reaching up to 300 mm after the case with a turbine undergoing a 30.6-hour-long icing event. Based on the icing similarity parameter concept and blade element momentum (BEM) theory along with the known geometric information of the turbine blades, a theoretical analysis was performed to predict the LE ice thickness distributions along the turbine blades. The theoretical predictions were found to agree with the field measurement data reasonably well.

In addition to utilizing the UAS-based imaging system to examine the characteristics of ice accretion on the turbine blades, supervisory control and data acquisition (SCADA) systems were also used to monitor the operational status and power production outputs of the wind turbines in terms of incoming wind speed measured at the turbine hub height, blade rotational speed, the pitch angle of the turbine blades, and the power production outputs of the wind turbines. The effects of the ice accretion on the turbine operation status and the power production capacities of the wind turbines were evaluated quantitatively by comparing the SCADA measurement data acquired during the icing events against those under normal operation conditions (i.e., without ice accretion). It was revealed clearly that, since the ice accretion on turbine blades would degrade the aerodynamic performance of the turbine blades significantly, much smaller torques could be generated by the iced turbine blades, despite the high incoming wind speed during the icing event. As a result, the wind turbines were found to rotate much slower and even shut down frequently due to the lack of sufficient torques to drive the turbines to rotate. Therefore, the measured power production outputs of the wind turbines during the icing events were found to become significantly lower than those under normal operation conditions (i.e., without ice accretion). While the icing-induced power production losses were found to be closely related to the length of the icing duration the turbines experienced, the averaged power production loss induced by ice accretion was found to reach up to 80% for the case with a wind turbine over the 30-hour-long icing event.

Authorship contribution statement

Linyue Gao: field measurements, data acquisition and processing, formal analysis, Writing - original draft.

Tao: field measurements, data acquisition and processing.

Yongqian Liu: methodology, draft review, funding acquisition, supervision.

Hui Hu: conceptualization, methodology, formal analysis, writing – review & editing, funding acquisition, supervision.

Declaration of competing interest

The authors declare that they do not have any known competing interests that could have appeared to influence the work reported in this paper.

Acknowledgments

This research work is partially supported by Iowa Energy Center for Wind Turbine Icing Study under the IEC Competitive Grant # 312350 and National Science Foundation (NSF) under award numbers of OISE-1826978 and CBET-1916380. The assistance from Mr. Zhicheng Hou of Nanjing Zhongren Energy Technology Co., LTD in conducting the field measurements, is also gratefully acknowledged.

References

[1] V. Lehtomäki, Wind Energy in Cold Climates Available Technologies - Report, 2016.
[2] M.B. Bragg, A.P. Broeren, L.A. Blumenthal, Iced-airfoil aerodynamics, Prog. Aero. Sci. 41 (2005) 323–362, https://doi.org/10.1016/j.paerosci.2005.07.001.
[3] L. Gao, Y. Liu, W. Zhou, H. Hu, An experimental study on the aerodynamic performance degradation of a wind turbine blade model induced by ice accretion process, Renew. Energy 133 (2019) 663–675, https://doi.org/10.1016/J.RENENE.2018.10.032.
[4] A.G. Kraj, E.L. Bibeau, Phases of icing on wind turbine blades characterized by ice accumulation, Renew. Energy 35 (2010) 966–972, https://doi.org/10.1016/j.renene.2009.09.013.
[5] D.B. Stoyanov, J.D. Nixon, Alternative operational strategies for wind turbines in cold climates, Renew. Energy 145 (2020) 2694–2706, https://doi.org/10.1016/j.renene.2019.08.023.
[6] T. Wallenius, V. Lehtomäki, Overview of cold climate wind energy: challenges, solutions, and future needs, Wiley Interdiscipl. Rev. Energy Environ. 5 (2016) 128–135, https://doi.org/10.1002/wene.170.
[7] W.J. Jasinski, S.C. Noe, M.S. Selig, M.B. Bragg, Wind turbine performance under icing conditions, J. Sol. Energy Eng. 120 (1998) 60, https://doi.org/10.1115/1.2888048.
[8] C. Hochart, G. Fortin, J. Perron, A. Ilinca, Wind turbine performance under icing conditions, Wind Energy 11 (2008) 319–333, https://doi.org/10.1002/we.258.
[9] H. Seifert, Technical requirements for rotor blades operating in cold climate, in: Proc. Boreas VI, 2003, pp. 50–55.
[10] M.C. Homola, P.J. Nicklasson, P.A. Sundsbø, Ice sensors for wind turbines, Cold Reg. Sci. Technol. 46 (2006) 125–131.
[11] V. Daniliuk, Y. Xu, R. Liu, T. He, X. Wang, Ultrasonic de-icing of wind turbine blades: performance comparison of perspective transducers, Renew. Energy 145 (2020) 2005–2018, https://doi.org/10.1016/j.renene.2019.07.102.
[12] O. Fakorede, Z. Feger, H. Ibrahim, A. Ilinca, J. Perron, C. Masson, Ice protection systems for wind turbines in cold climate: characteristics, comparisons and analysis, Renew. Sustain. Energy Rev. 65 (2016) 662–675, https://doi.org/10.1016/j.rser.2016.06.080.
[13] L. Gao, Y. Liu, H. Hu, An experimental investigation of dynamic ice accretion process on a wind turbine airfoil model considering various icing conditions, Int. J. Heat Mass Tran. 133 (2019) 930–939, https://doi.org/10.1016/J.IJHEATMASSTRANSFER.2018.12.181.
[14] L. Gao, Y. Liu, H. Hu, An experimental investigation on the dynamic glaze ice accretion process over a wind turbine airfoil surface, Int. J. Heat Mass Tran. 149 (2020) 119120, https://doi.org/10.1016/J.IJHEATMASSTRANSFER.2019.119120.
[15] L. Gao, R. Veerakumar, Y. Liu, H. Hu, Quantification of the 3D shapes of the ice structures accreted on a wind turbine airfoil model, J. Vis. 22 (2019) 661–667, https://doi.org/10.1007/s12650-019-00567-4.
[16] P. Blasco, J. Palacios, S. Schmitz, Effect of icing roughness on wind turbine power production, Wind Energy 20 (2017) 601–617, https://doi.org/10.1002/we.2026.
[17] F. Lamraoui, G. Fortin, R. Benoit, J. Perron, C. Masson, Atmospheric icing impact on wind turbine production, Cold Reg. Sci. Technol. 100 (2014) 36–49, https://doi.org/10.1016/j.coldregions.2013.12.008.
[18] M.C. Pedersen, H. Sørensen, Towards a CFD Model for Prediction of Wind Turbine Power Losses Due to Icing in Cold Climate, 2016, pp. 1–6.
[19] A. Zanon, M. De Gennaro, H. Kühnelt, Wind energy harnessing of the NREL 5 MW reference wind turbine in icing conditions under different operational strategies, Renew. Energy 115 (2018) 760–772, https://doi.org/10.1016/j.renene.2017.08.076.
[20] O. Parent, A. Ilinca, Anti-icing and de-icing techniques for wind turbines: critical review, Cold Reg. Sci. Technol. 65 (2011) 88–96, https://doi.org/10.1016/j.coldregions.2010.01.005.
[21] L. Gao, Y. Liu, L. Ma, H. Hu, A hybrid strategy combining minimized leading-edge electric-heating and superhydro-/ice-phobic surface coating for wind turbine icing mitigation, Renew. Energy 140 (2019) 943–956, https://doi.org/10.1016/J.RENENE.2019.03.112.
[22] E. Rindeskär, Modelling of Icing for Wind Farms in Cold Climate : A Comparison Between Measured and Modelled Data for Reproducing and Predicting Ice Accretion, Dep. Earth Sci., 2010, pp. 1–54.
[23] L. Shu, H. Li, Q. Hu, X. Jiang, G. Qiu, G. McClure, H. Yang, Study of ice accretion feature and power characteristics of wind turbines at natural icing environment, Cold Reg. Sci. Technol. 147 (2018) 45–54, https://doi.org/10.1016/j.coldregions.2018.01.006.
[24] A. Chehouri, R. Younes, A. Ilinca, J. Perron, Review of performance optimization techniques applied to wind turbines, Appl. Energy 142 (2015) 361–388, https://doi.org/10.1016/j.apenergy.2014.12.043.
[25] W. Yang, R. Court, J. Jiang, Wind turbine condition monitoring by the approach of SCADA data analysis, Renew. Energy 53 (2013) 365–376, https://doi.org/10.1016/j.renene.2012.11.030.
[26] A. Zaher, S.D.J. McArthur, D.G. Infield, Y. Patel, Online wind turbine fault detection through automated SCADA data analysis, Wind Energy 12 (2009) 574–593, https://doi.org/10.1002/we.319.
[27] P. Sun, J. Li, C. Wang, X. Lei, A generalized model for wind turbine anomaly identification based on SCADA data, Appl. Energy 168 (2016) 550–567, https://doi.org/10.1016/j.apenergy.2016.01.133.
[28] Y. Liu, L. Li, Z. Ning, W. Tian, H. Hu, Experimental investigation on the dynamic icing process over a rotating propeller model, J. Propul. Power (2018) 1–15, https://doi.org/10.2514/1.B36748, 0.
[29] R.M. Waldman, H. Hu, High-speed imaging to quantify transient ice accretion process over an airfoil, J. Aircraft 53 (2016) 369–377, https://doi.org/10.2514/1.C033367.
[30] L. Battisti, Wind Turbines in Cold Climates, Springer International Publishing, Cham, 2015, https://doi.org/10.1007/978-3-319-05191-8.
[31] D. Anderson, Acceptable tolerances for matching icing similarity parameters in scaling applications, in: 39th Aerosp. Sci. Meet. Exhib, American Institute of Aeronautics and Astronautics, 2001, https://doi.org/10.2514/6.2001-832.
[32] Y. Han, J. Palacios, S. Schmitz, Scaled ice accretion experiments on a rotating wind turbine blade, J. Wind Eng. Ind. Aerod. 109 (2012) 55–67, https://doi.org/10.1016/j.jweia.2012.06.001.
[33] D.A. Johnson, M. Gu, B. Gaunt, Wind turbine performance in controlled conditions: experimental results, Int. J. Green Energy (2016), https://doi.org/10.1080/15435075.2012.675799 (2012) null-null.
[34] M. Arifujjaman, M.T. Iqbal, J.E. Quaicoe, Reliability analysis of grid connected small wind turbine power electronics, Appl. Energy 86 (2009) 1617–1623, https://doi.org/10.1016/j.apenergy.2009.01.009.